Combustion and Flame 237 (2022) 111842

Contents lists available at ScienceDirect

Combustion and Flame

journal homepage: www.elsevier.com/locate/combustflame

Distortion of expanding *n*-heptane flames at high unburned-gas temperatures behind reflected shocks

Adam J. Susa*, Ronald K. Hanson

Department of Mechanical Engineering, Stanford University, 452 Escondido Mall, Stanford, CA 94305 USA

ARTICLE INFO

Article history:
Received 1 July 2021
Revised 17 October 2021
Accepted 17 October 2021

Keywords:
Shock tube
Heptane
Premixed flames
Imaging,

ABSTRACT

Simultaneous, dual-perspective, high-speed imaging is used to provide new insight into the morphology of flames generated at high unburned-gas temperatures behind reflected shock waves. Single-perspective, end-wall imaging left previous applications of the shock-tube flame speed method reliant on an assumption of axial symmetry when interpreting experimental results. Here, we report qualitative and quantitative observations from the first application of simultaneous side- and end-wall emission imaging to characterize the three-dimensional morphology of these flames. Side-wall imaging reveals that, while the expected flame symmetry is observed under static and relatively low temperature post-reflected-shock conditions, symmetry can break down at higher temperatures. These results reveal that the concentric regions of emission previously observed in flame experiments in the negative-temperature-coefficient ignition regime can be explained as the axial integration of emission through a distorted flame. Several physical mechanisms are evaluated towards the goal of identifying the underlying cause of flame distortion. The post-reflected-shock flow field and pressure-wave–flame interactions are both found insufficient to explain the results. Presently, not enough is known about the recently identified local-double-flame structure to assess the likelihood of its relevance in the present experiments. As such, while the dual-perspective imaging results provide important new insight into the morphology of high-temperature flames and inform the correct interpretation of previous experimental observations, the specific mechanism leading to the observed distortion remains a topic requiring further attention.

1. Introduction

The shock tube has been long regarded as a preferred, zero-dimensional apparatus for the study of chemical kinetics at high temperatures [1–4]. Nevertheless, it was not until the recent work of Ferris et al. that the application of shock tubes to enable the study of laminar flames at high unburned-gas temperatures (T_u) was first leveraged [5].

To avoid disrupting the shock-tube flow field, non-intrusive laser-induced breakdown is used to ignite flames in the post-reflected-shock (region-5), unburned-gas environment. Plasma kernels generated through laser-induced breakdown, their associated flow fields, and flames ignited from such plasmas are all commonly treated as axis-symmetric about the path of the igniting laser beam [e.g. 6, 7,8, 9]. Applied to shock-tube flame experiments, this assumption is a basis for the aspherical correction reported by Ferris et al. [5] and is implicit in the multi-stage flame structure previously hypothesized as a possible explanation for the concentric rings of emission observed in end-wall images of *n*-heptane and *iso*-octane flames at temperatures associated with low-temperature ignition chemistry [10–12].

Multiple imaging diagnostics have been developed for shock-tube experiments over the past decades. Early realizations of side-wall imaging employed schlieren photography in rectangular shock tubes to explore shock-induced autoignition [e.g. 13–15]. Side-wall schlieren was later extended to round shock tubes utilizing configurations either consisting of an optical shock-tube section designed as an acylindrical lens [16] or containing flat windows [17,18]. End-wall emission imaging in a round shock tube was developed by Troutman et al. [19] and has been used in prior works employing the shock-tube flame speed method [e.g. 5,10,11]. Extensions of emission and fluorescence imaging to the side wall of a round shock tube have employed windows designed as zero-power cylindrical lenses [20] and a custom endoscope installed in a diagnostic port [21]. Most recently, simultaneous end- and side-wall emission imaging of spontaneous ignition behind reflected shock waves

* Corresponding author.
E-mail address: asusa@stanford.edu (A.J. Susa).

https://doi.org/10.1016/j.combustflame.2021.111842
0010-2180/

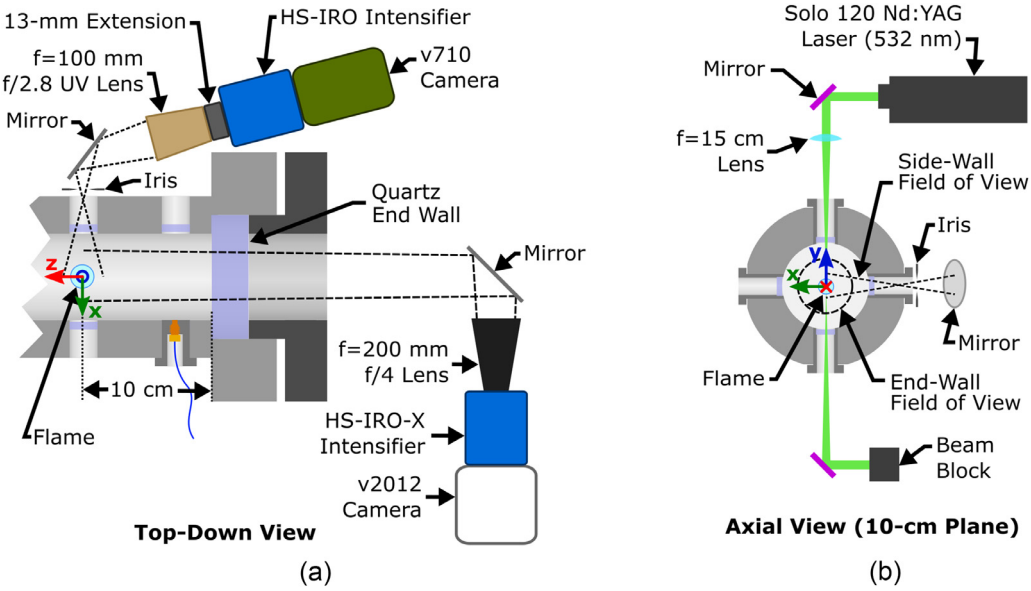

Fig. 1. Schematic of the instrumentation used in this work, as viewed a) from the top and b) from the end of the tube. The shock tube is shown in cross section. The ignition laser in (a) and cameras in (b) are out of plane and not shown for clarity. Schematic not to scale; imaging ray tracing is approximate.

has been realized in round shock tubes using flat [22] and annular [23] side-wall windows.

In this work, simultaneous side- and end-wall emission imaging is applied to expanding-flame experiments in a shock-tube, providing the first characterization of the three-dimensional (3-D) morphology of flames at high unburned-gas temperatures. Unlike prior realizations of side-wall imaging in a round shock tube that required custom optics [21] or shock-tube modifications to accommodate special side-wall windows [16,17,20,22,23], this work demonstrates side-wall emission imaging using standard optical components and a conventional side-wall diagnostic port. Observations reported here provide a revised understanding of high-temperature shock-tube flame experiments, wherein axial distortion provides a likely explanation for previously reported flame structure consisting of concentric rings of emission.

2. Experimental methods

High-temperature expanding-flame experiments were performed in a stainless-steel, 11.5-cm-inner-diameter shock tube, a facility described in detail by Campbell et al. [24]. A dual-camera imaging configuration was devised to perform simultaneous side-wall and end-wall imaging (Fig. 1). A quartz end-wall window provides axial optical access [19]. End-wall emission images are recorded by a Phantom v2012 camera (Vision Research) paired with an ultraviolet (UV)-sensitive, high-speed intensified relay optic (HS-IRO-X, LaVision). In static experiments, images are recorded through a 105-mm UV-Nikkor lens at 85.2 pixel-per-cm resolution, providing a FOV greater than 10 cm at 20,000 frame-per-second (fps). For reflected-shock experiments, a 200-mm-focal-length, f/4 Nikkor lens is used, providing a 7-cm field of view (FOV) at a higher resolution of 124 pixels per cm and the same frame rate.

A side-wall imaging system is configured through the 1.8-cm-diameter diagnostic port available in the shock tube. In order to maximize the FOV at the center of the shock tube, a UV-transparent lens with 100-mm focal length and f/2.8 aperture (Sodern Cerco) is used. The lens is offset from the intensifier by a 13-mm extension ring and focused to produce a hypercentric optical arrangement. An iris is positioned just outside the side-wall plug to restrict the collection angle of light and flatten the spatial intensity profile observed at the in-tube focal plane. With this arrangement, and the intensification provided by a HS-IRO (LaVision) to compensate for the low collection efficiency, a FOV of about 2.5 cm is realized. Images are recorded by a Phantom v710 camera (Vision Research) at 20,000 fps synchronized with the end-wall camera. By the Scheimpflug principle, and considering the side-wall camera and mirror angles, the focal plane within the shock tube will be slightly misaligned from the Y-Z plane [25,26]. This results in a corresponding spatial resolution variation across the FOV (185–197 pix/cm), as determined using a calibration image of a ruler positioned in the Y-Z plane. The nominal value of 191 pix/cm is used for the side-wall resolution in the remainder of this work, with the variation representing an uncertainty of about ±3%. While this uncertainty is negligible for the purposes of the present work, it is noted here as it should be treated in detail if similar optical arrangements are used for high-precision flame speed measurements in the future.

The flame is initiated behind the reflected shock wave by a plasma spark generated through laser-induced breakdown [5]. A flash-lamp-pumped, Q-switched, neodymium-doped yttrium aluminum garnet (Nd:YAG) laser (Solo PIV 120, New Wave Research) is used as the ignition-laser source. This laser is internally frequency doubled to 532nm and produces quoted pulse lengths of 3–5 ns. The beam is focused by a 15-cm-focal-length, best-form bispherical lens and enters the tube vertically though an optical port 10 cm from the driven-section end wall and perpendicular to the port through which side-wall imaging is performed. The focused beam forms a waist at the center of the tube where laser-induced breakdown occurs, igniting an expanding flame. The Q-switch timing relative to the flash lamp is varied to control the energy of the laser pulse. While it could not be directly measured during experiments, the spark energy is estimated from offline measurements to be in the range 5–10 mJ for experiments reported in this study.

Fuel and oxidizer test-gas mixtures are prepared manometrically in a stainless-steel mixing tank from research-grade components. The mixture is allowed to homogenize for at least one hour with agitation from a mechanically driven mixing vane prior to being introduced into the tube. In static experiments, the constrained-reaction-volume (CRV) gate valve [24] is closed, isolating the 40 cm of the shock tube nearest the end wall as a constant-volume cylindrical combustion chamber, as was reported in simi-

lar validation experiments with end-wall imaging by Ferris et al. [5]. This isolated section is filled to the desired pressure at ambient temperature (~296 K), and the laser and camera are simultaneously triggered to ignite and record a flame under quiescent conditions.

In reflected-shock experiments, the test-gas fill pressure (P_1), driver pressure (P_4), and driver composition (a mixture of N_2 and He) are jointly selected in order to generate shock waves of different incident mach numbers. Simultaneous adjustment of both pressures and the composition is required to reach different post-reflected-shock, region-5, unburned-gas temperatures ($T_5 = T_u$) while maintaining a post-shock, unburned-gas pressures ($P_5 = P_u$) near 1.25 atm (± 10%) across shocked experiments of differing T_5.

Following diaphragm rupture, passage of the resulting shock wave is recorded by PCB pressure transducers at precisely known locations. These records provide a measure of the incident shock velocity, from which the post-reflected-shock conditions are calculated using normal-shock relations. In applying the shock-jump equations, it is assumed that vibrational equilibrium is reached in the post-incident-shock (region-2) gas, an assumption supported by the use of helium diluent and relatively high fuel loading in the unburned-gas mixture [27]. The timing of the ignition laser and cameras are controlled through external triggering relative to the shock passing an upstream PCB. In the reflected-shock experiments reported in this work, flames were ignited about 1.1 ms following passage of the reflected shock wave; this is comparable to the shortest spark delay time (0.9 ms) in a previous study in which concentric regions of emission were reported [11].

3. Data interpretation

From each image sequence, radius and observed flame-propagation velocity measures are extracted to inform the quantitative discussion in Section 5. Radii are extracted from each image along the major axes using a binarization-based method implemented in the open-source Python programming language [28] and using the Scikit-Image [29] and Scipy [30] packages (Fig. 2). A Gaussian filter with a standard deviation of 1.5 pixels is first applied to the images to reduce pixel-level noise (Fig. 2b). Images are then binarized using a hysteresis thresholding method [31]; high and low threshold values are taken as the respective threshold values from a dual-threshold multi-Otsu method [32]. The binary images are then cleaned using a sequence of operations to label and remove small regions from the images [33] and perform a morphological closing as a sequence of dilation, hole filling, and erosion operations using a disk-shaped kernel of radius five pixels (Fig. 2c).

The radius of the flame, $R_{f,j}$, along each major axis (j = x, y, z; see Fig. 1) is defined as half the total extent, D_j, of the binary region along that axis (Fig. 2c),

$$R_{f,j} = \frac{D_j}{2} = \frac{(i_{j,\max} - i_{j,\min})}{2}\mathcal{S}. \tag{1}$$

Here, i_j's are pixel indices along axis j over which the flame extends and $\mathcal{S}$ is the physical scale of the image (units of cm/pixel) determined from a calibration image. Following this process, x and y radii can be extracted from end-wall images, and y and z radii are available from side-wall images.

Once radii are determined (Fig 3a, symbols), the observed flame propagation speed, $S_{f,j}$, is defined relative as the time derivative of the radius,

$$S_{f,j} = \frac{\mathrm{d}R_{f,j}}{\mathrm{d}t}. \tag{2}$$

Raw radii data are first smoothed used a Savizty-Golay filter [34] to locally fit a second-order polynomial to a centered window of 7 data points (Fig 3a, line). Smoothed data are then differentiated using a first-derivative Savizty-Golay filter in order to reduce the impact of random noise on the computed $S_{f,j}$ values (Fig 3b).

As seen in Fig. 3, and is typical of the experiments reported here, close agreement is observed between the matched Y-axis radii and flame-speeds measurements obtained from the two perspectives, exhibiting only small discrepancies. One possible cause of mismatch between the perspectives arises from uncertainty in the image-scale calibration, which would manifest as a constant scaling factor between the Y-axis measurements. Another factor is that differences in the imaging systems' response to emission from the flame could result in slightly different locations on the flame being identified as the flame front location by the binarization routine when applied to images from different perspectives. A final factor results from the hypercentric side-wall imaging arrangement, which features a strongly diverging imaging FOV through the shock tube (Fig. 1). This results in a side-wall magnification that varies more strongly with working distance than that of the end-wall camera. As a result, the effective physical scaling of the side-wall images would be expected to increase as the flame grows, an effect discussed by Halter et al. applied to imaging of flames in an optically accessible constant-volume vessel [35].

The primary interest of the quantitative analysis included in this work is to provide for comparison across the measurements obtained along each of the three axes. As such, it is desirable to correlate the side- and end-wall measurements in such a way as to minimize the impacts of the non-ideal effects introduced above. If the assumption is made that the non-ideality of the hypercentric, side-wall imaging arrangement is greater than that of the end-wall system, the desirable outcome would then be to correct the side-wall images to be directly comparable to those obtained from the end wall. Furthermore, by assuming the various non-ideal effects affect the Y- and Z-axis measurements equivalently, corrected side-wall radii measurements, $R^{\star}_{f,j}$, can be defined by scaling the side-wall measurements by the ratio of the end- and side-wall Y-axis measurements,

$$R^{\star}_{f,y} = R_{f,y|sidewall}\left(\frac{R_{f,y|endwall}}{R_{f,y|sidewall}}\right) \equiv R_{f,y|endwall} \tag{3}$$

$$R^{\star}_{f,z} = R_{f,z|sidewall}\left(\frac{R_{f,y|endwall}}{R_{f,y|sidewall}}\right). \tag{4}$$

In this manner, the duplicated Y-axis measurements are collapsed to a single result (that from the end wall), and the side-wall Z-axis measurement is scaled to be comparable to the end-wall results. The effect of applying Eqs. (3) and (4) to the radii results of Fig. 3 are shown in Fig. 4, which presents a single, unified set of 3-axis radii and propagation speed measurements.

In the ideal limit of a spherical flame and stagnant burned gas, $S_{f,j}$ would correspond exactly to the burned flame speed, S_b [36]. However, non-ideal effects can manifest as perturbations to the radius occurring at rate $\dot{\mathcal{R}}_{f,j}$, such that the $S_{f,j}$ observed results from a combination of S_b and $\dot{\mathcal{R}}_{f,j}$,

$$S_{f,j} = S_b + \dot{\mathcal{R}}_{f,j} \tag{5}$$

$$S_b = S_{f,j} - \dot{\mathcal{R}}_{f,j}. \tag{6}$$

Here, positive $\dot{\mathcal{R}}_{f,j}$ indicates the flame is being stretched along axis j, leading to observed propagation speed $S_{f,j}$ to exceed the actual burned flame speed, S_b. If the flame is instead compressed, $\dot{\mathcal{R}}_{f,j}$ will be negative, leading to $S_{f,j} < S_b$. This formulation will be revisited in the discussion of Section 5.1 to assess the extent to which flow-field effects are able to explain observed distortion.

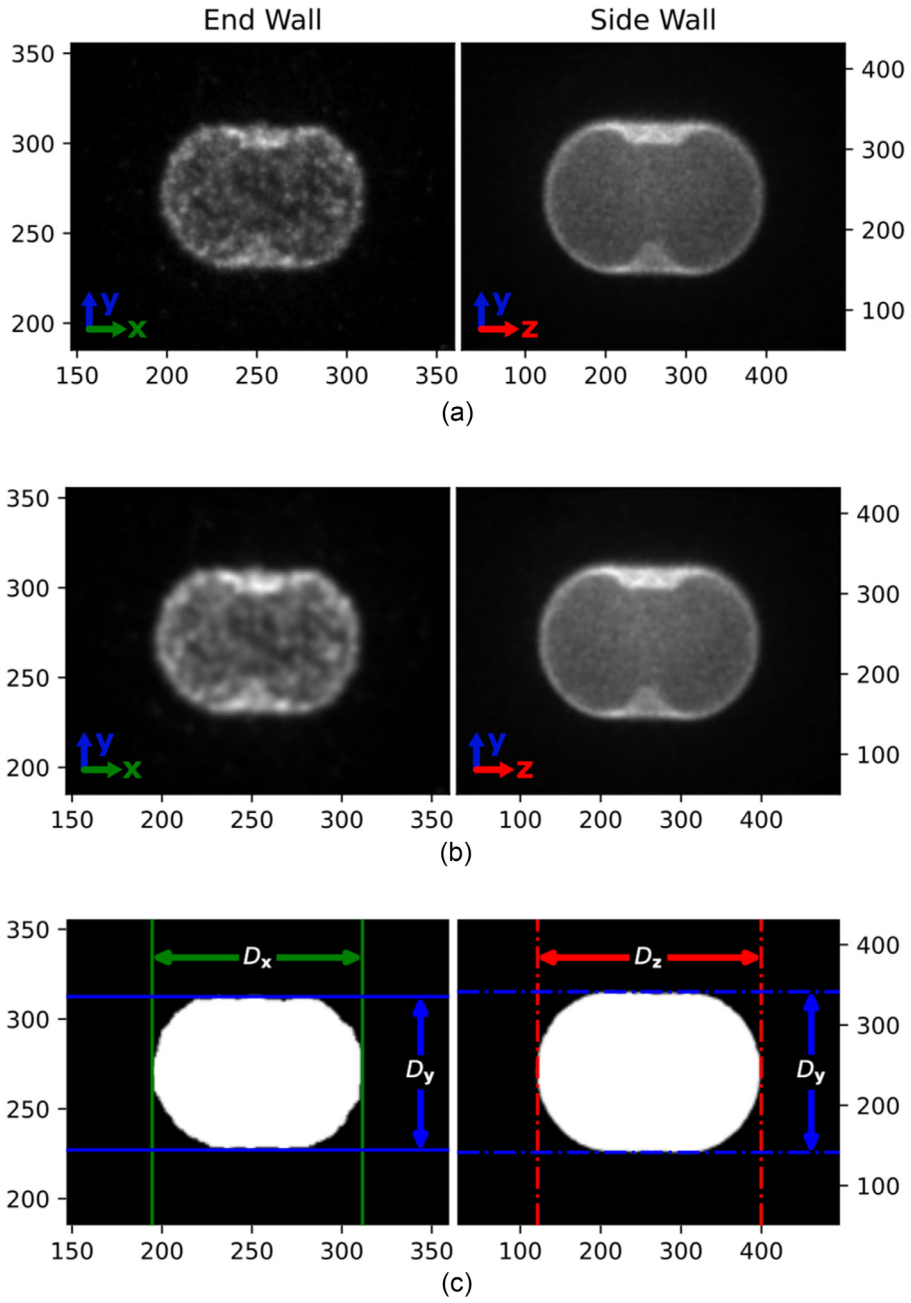

Fig. 2. Example image pair recorded 1 ms after the spark during a static experiment illustrating the image processing procedure: (a) raw emission images, (b) Gaussian smoothed images, and (c) clean binary images. Axis scales are in units of pixels; select 2.5-cm by 2-cm regions are shown for both perspectives, centered about the flame. Experimental conditions: T_u = 296 K, P_u = 0.5 atm, unburned-gas composition = 0.056 C_3H_8, 0.200 O_2, 0.744 Ar.

4. Results

The dual-perspective imaging configuration provides the first opportunity to evaluate the 3-D morphology of flames ignited in a shock tube. In Section 4.1, simultaneous side- and end-wall imaging are first demonstrated in static-flame experiments to validate the experimental configuration in a fully quiescent environment. Section 4.2 subsequently presents results obtained of flames ignited behind reflected shock waves at high unburned-gas temperatures.

In all image sets that follow, end-wall images (left column) are scaled and cropped to match the resolution and FOV of the side-wall images (right column). Limiting the end-wall FOV in this way restricts the maximum flame radius considered to about 30% that of the vessel, the criteria put forth by Burke et al. as necessary to avoid the impact of cylindrical-confinement effects on expanding flames [37]. Videos containing additional frames and displaying a larger end-wall FOV are provided in the supplemental materials for each experiment[1]

4.1. Static-flame characterization

Results obtained from expanding flame experiments performed with static unburned gas in the isolated CRV section are presented

[1] The top and bottom of the side-wall images in the supplemental materials are padded with zeros (i.e. black) to match the vertical extent of the end-wall perspective.

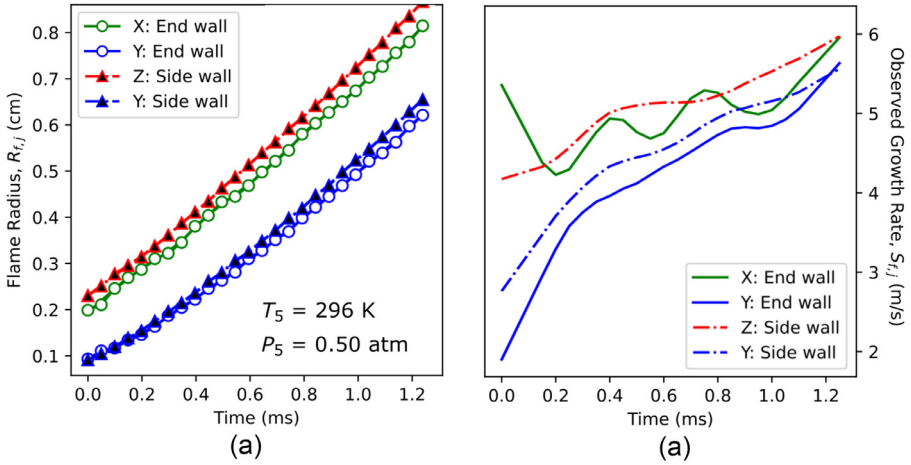

Fig. 3. (a) Radii and (b) observed flame propagation data extracted from a static experiment. Experimental conditions: T_u = 296 K, P_u = 0.5 atm, unburned-gas composition = 0.056 C_3H_8, 0.200 O_2, 0.744 Ar.

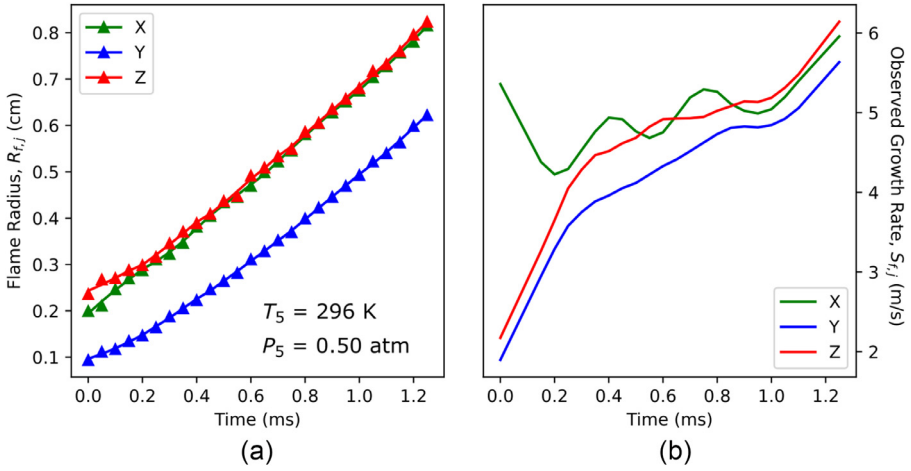

Fig. 4. (a) Corrected radii and (b) observed flame propagation data extracted from a static experiment. Experimental conditions: T_u = 296 K, P_u = 0.5 atm, unburned-gas composition = 0.056 C_3H_8, 0.200 O_2, 0.744 Ar.

in Fig. 5. The unburned-gas mixture consisted of propane (C_3H_8) at a slightly lean equivalence ratio (ϕ = 0.98) in an oxidizer comprised of 21% O_2 and 79% Ar. Experiments were performed at ambient T_u (296 K) and sub-atmospheric and elevated P_u (Fig. 5 a and b, respectively). Radii and flame speed results for the sub-atmospheric case are presented in Fig. 4 and dummyTXdummy- for elevated pressure in Fig. 6.

In both experiments, the flames appear nearly identical in both the end-wall and side-wall views. End-wall images appear more grainy due to the lower spatial resolution of the end-wall camera configuration and the use of an older image intensifier. The close agreement between the measured X and Z radii and propagation velocities are in keeping with the established theory and expectations of symmetry about the laser (Y) axis for a laser-ignited flame in a quiescent environment. This result demonstrates that no significant asymmetry is present in the plasma spark generated by the current optical configuration that would inherently introduce asymmetry into the resulting flame.

While the energies of the ignition laser pulses were closely matched in the two experiments (within 10%), the elevated pressure flame develops a lobe at the top of the flame, the side from which the ignition beam enters, whereas the flame at lower pressure transitions smoothly from a toroidal flame to one of an elongated shape. This difference is understood to be indicative of a higher spark energy at elevated P_u, resulting from the absorption of a greater portion of the laser energy owing to a reduction of the laser breakdown threshold at increased pressure [38]. Whereas the *Y*-axis radius in the low-pressure flame is persistently lower than the *X*- and *Z*-axis measurements (Fig. 4a), the third lobe has the effect in the high-pressure flame of making up for this deficiency, such that close agreement in the radii and propagation speeds is seen across all three axes (Fig. 6).

4.2. Reflected-Shock experiments

Figure 7 shows a comparison of select end- and side-wall images of flames ignited behind reflected shock waves at three different T_5 values. Lean *n*-heptane (ϕ = 0.9) in an oxidizer of 18% O_2, 41% He, and 41% Ar was used as the test-gas. The fuel–oxidizer mixture used in the shocked experiments was chosen to match that from a previous study in which concentric regions of emission were observed using end-wall imaging [11]. The driven-section end wall is to the left of the FOV in the side-wall images, such that the slight bulk motion of the flames occurs towards the end wall [39,40]. *Z*-axis radii and propagation speed data are truncated at the frame in which the flame first exceeds the side-wall FOV.

For all three flames shown in Fig. 7, the initial flame kernels (top row) appear the same in the end- and side-wall images. This observation indicates that the expected axisymmetric ignition-kernel structure is realized immediately following ignition at all

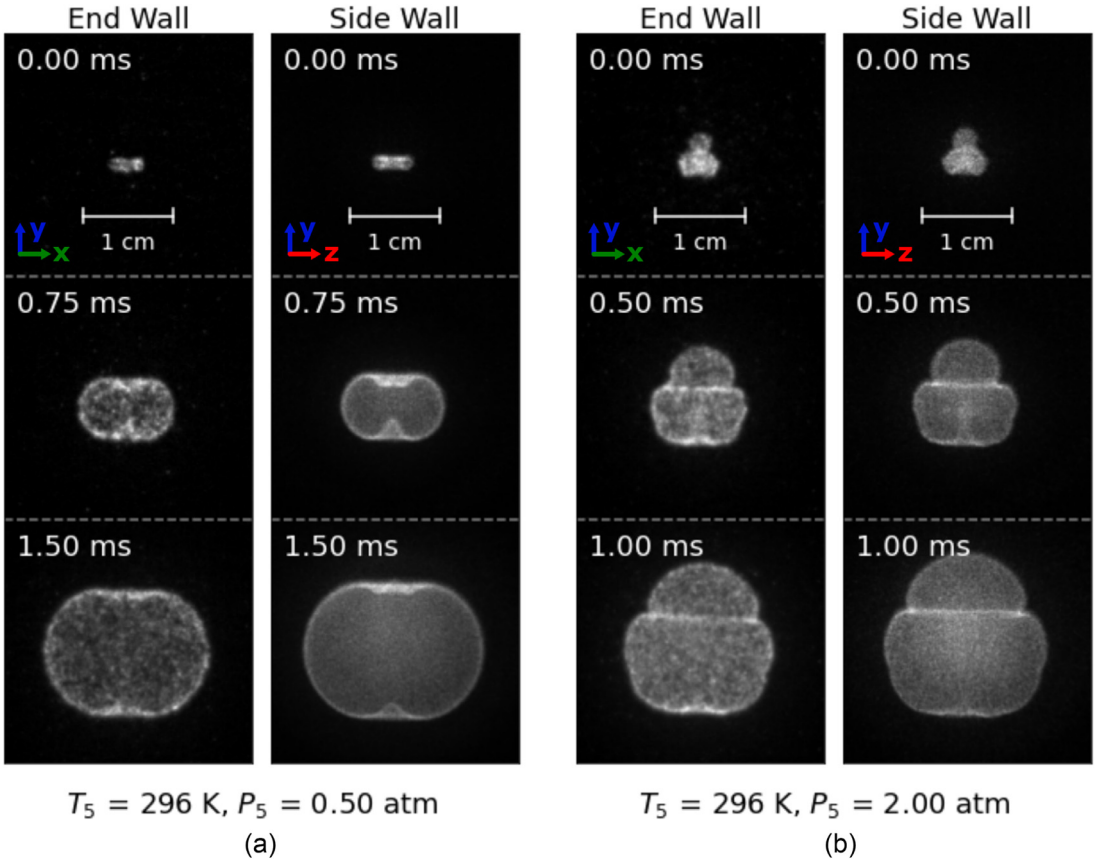

Fig. 5. Select frames comparing the flame morphology in static experiments as seen in end- and side-wall images. Flames are observed to be axis-symmetric at both (a) sub-atmospheric and (b) elevated pressure. Labeled times are relative to the first frame following the ignition spark. Unburned-gas composition: 0.056 C_3H_8, 0.200 O_2, 0.744 Ar.

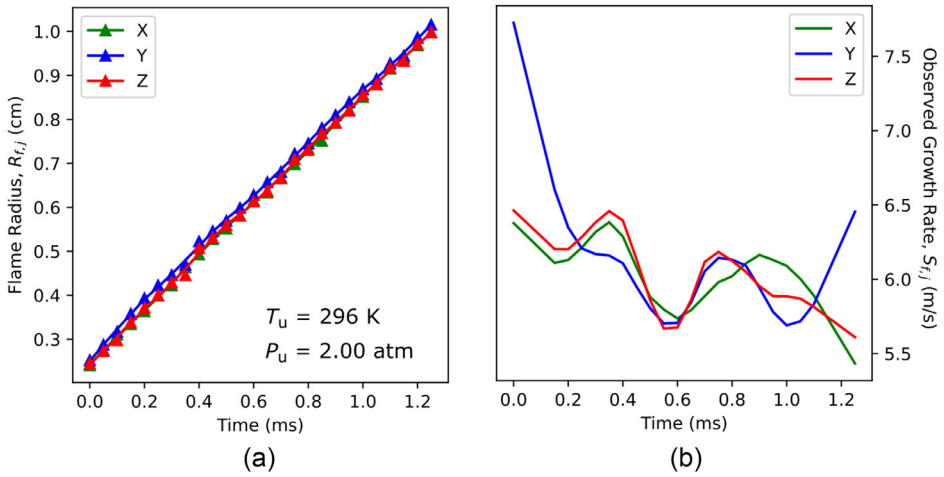

Fig. 6. (a) Corrected radii and (b) observed flame propagation data extracted from a static experiment. Experimental conditions: T_u = 296 K, P_u = 2.0 atm, unburned-gas composition = 0.056 C_3H_8, 0.200 O_2, 0.744 Ar.

conditions shown, consistent with theory and the static results. At the lowest unburned-gas temperature (T_5 = 673 K, Fig. 7a), the flame is observed to maintain its symmetric appearance throughout its first 1 ms of growth. This qualitative observation is similarly borne out in the quantitative results (Fig. 8), which show close agreement between the X- and Z-radii up until the flame exceeds the side-wall FOV at 0.5 ms, indicative of axial symmetry; close agreement in the X- and Y-speeds at later times suggest flame propagation becomes quasi-steady as the flame grows.

The higher-temperature flames are both seen in the images to become distorted as they propagate. In Fig. 7b, the flame rapidly loses symmetry in the Z direction, flattening on the left side and forming an extended lobe on the right. While the presence of this distortion would not be immediately obvious in the quantitative results (Fig. 9), when viewed from the end-wall perspective, the axial integration of the distorted structure leads to the appearance of an inner, bright ring and outer annulus of emission. This observation is consistent with the regions of concentric emission

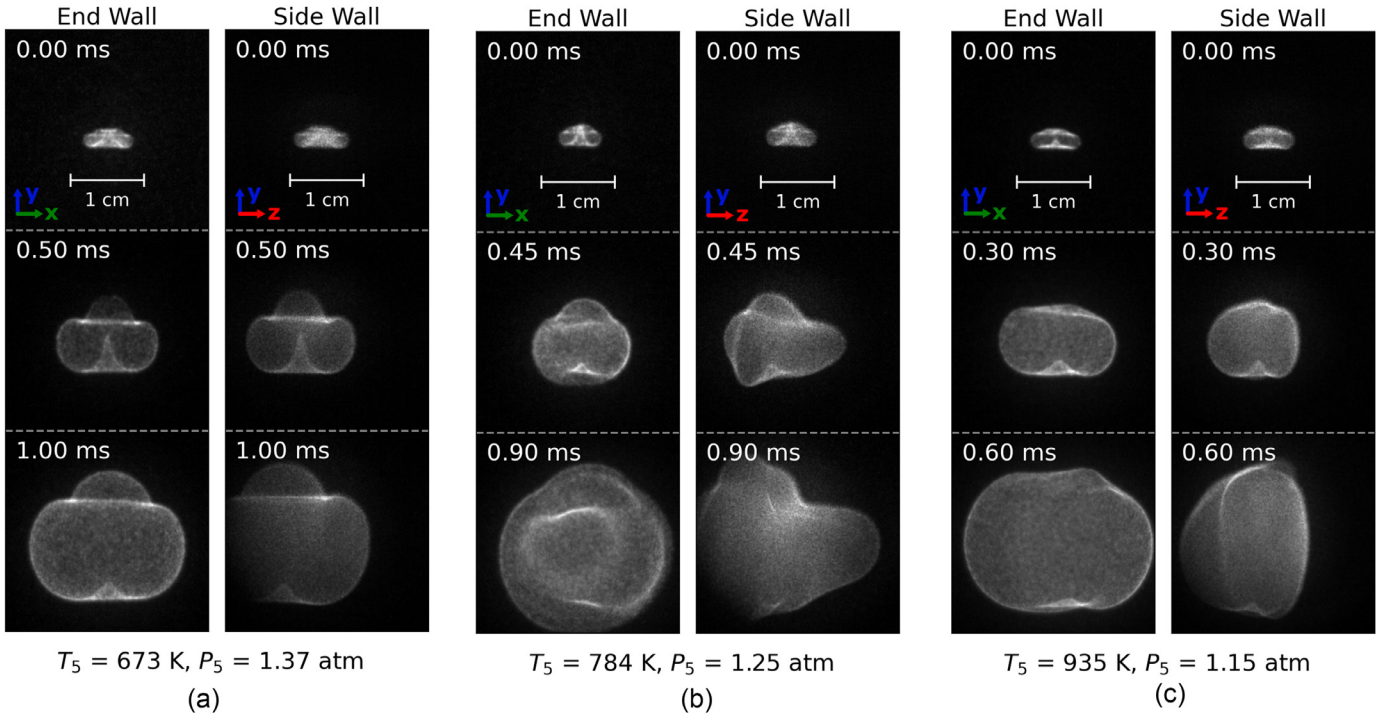

Fig. 7. Select frames comparing the flame morphology as seen in end- and side-wall images. a) Axis-symmetry flame at T_5 = 673 K, b) highly distorted flame at T_5 = 784 K, and c) axially compressed flame at T_5 = 935 K. Labeled times are relative to the first frame following the ignition spark. Unburned-gas composition: 0.0145 n-C_7H_{16}, 0.1780 O_2, 0.4030 Ar, 0.4015 He.

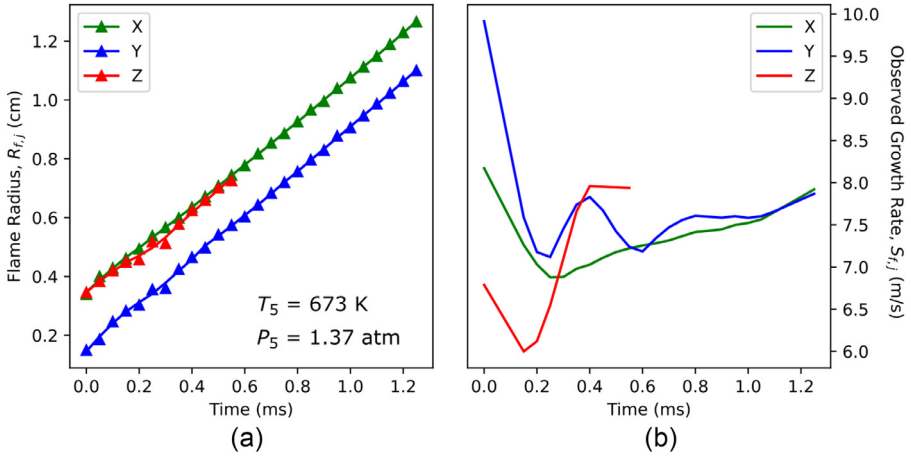

Fig. 8. (a) Corrected radii and (b) observed flame propagation data extracted from a shocked experiment at conditions T_5 = 673 K, P_5 = 1.37 atm, unburned-gas composition = 0.0145 n-C_7H_{16}, 0.1780 O_2, 0.4030 Ar, 0.4015 He.

reported in previous studies of *n*-heptane and *iso*-octane flames at comparable conditions in the negative-temperature-coefficient (NTC) ignition regime [10,11]. As such, while the repeatability of the distortion could not be explicitly evaluated in this work due to time constraints imposed by the use of a borrowed HS-IRO-X intensifier, the similarity between the present end-wall images and previous observations suggests comparable distortion occurs with some level of consistency.

Figure 7c, the flame with the highest T_5 shown, simultaneously displays horizontal (radial) stretching in the end-wall view and axial compression viewed from the side. In this case, the axial compression effect is clearly observable in the quantitative results (Fig. 10) as a deficit in $S_{f,z}$ on the order of 10 m/s relative to the velocity along the other two axes by the time the flame leaves the side-wall FOV at 0.6 ms. The horizontal (X-axis) stretching, meanwhile, is seen to be the result of both a larger initial $R_{f,x}$ and higher initial $S_{f,x}$.

5. Discussion

In an effort to understand the basic phenomena underlying the distortion observed in high-temperature flame experiments, three candidate mechanisms are discussed. First, the effect of superimposing a supposed post-reflected-shock flow field on an expanding flame is considered to determine the corresponding effect on the observed propagation rate (Section 5.1). Next, the refraction of a pressure wave with the discontinuity of the flame is presented as a mechanism for higher-order flow interaction effects (Section 5.2). Finally, the possibility of localized double-flame structures of po-

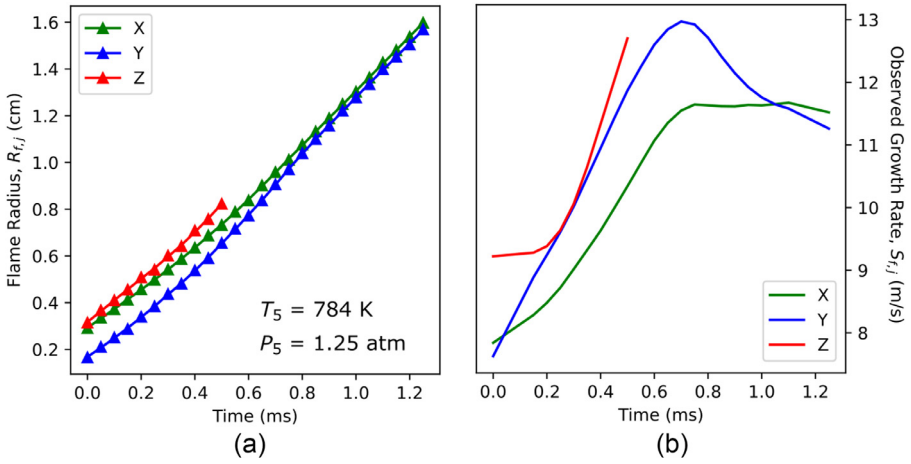

Fig. 9. (a) Corrected radii and (b) observed flame propagation data extracted from a shocked experiment at conditions T_5 = 784 K, P_5 = 1.25 atm, unburned-gas composition = 0.0145 n-C_7H_{16}, 0.1780 O_2, 0.4030 Ar, 0.4015 He.

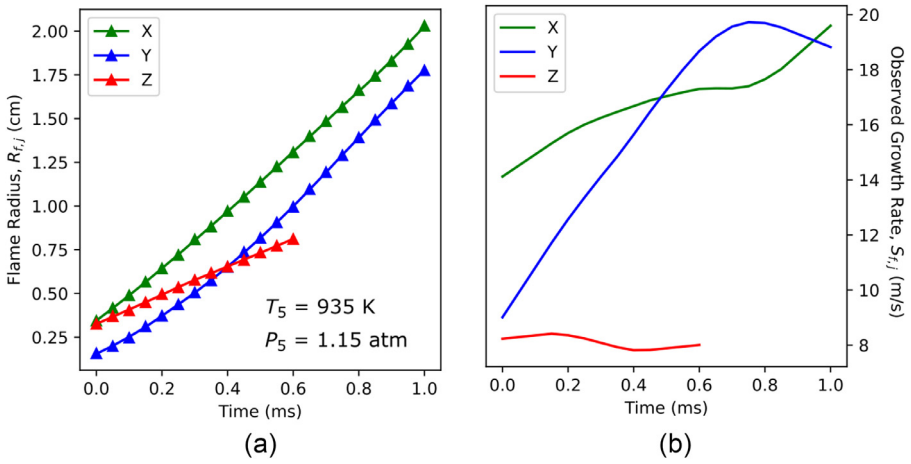

Fig. 10. (a) Corrected radii and (b) observed flame propagation data extracted from a shocked experiment at conditions T_5 = 935 K, P_5 = 1.15 atm, unburned-gas composition = 0.0145 n-C_7H_{16}, 0.1780 O_2, 0.4030 Ar, 0.4015 He.

tential relevance to the intermediate-temperature experiment is introduced based on preliminary simulation results (Section 5.3).

5.1. Post-reflected-shock flow field

Here, the ability of the post-reflected-shock flow field to account for the observed flame distortion is evaluated. In this discussion, the two separable components of the post-reflected-shock flow field are first considered individually. The magnitudes of the combined predicted flow-field effects on the observed flame propagation velocity are then compared to the discrepancy between the component velocities obtained from the highest-temperatures experimental results to evaluate the extent to which the flow field can account for the distortion.

5.1.1. Pressure-change induced flow

The rate at which the axial extent of a flame ignited behind a reflected shock varies as a result of isentropic pressure change in the region-5 gas can be predicted using the expression,

$$\frac{\mathrm{d}R_{\mathrm{f,z|dP}}}{\mathrm{d}t} = \frac{-R_{\mathrm{f,z}}}{\gamma_{\mathrm{u}}}\frac{1}{P}\frac{\mathrm{d}P}{\mathrm{d}t} \equiv \dot{\mathcal{R}}_{\mathrm{f,z|dP}}, \tag{7}$$

where $R_{\mathrm{f,z}}$ is the flame radius measured in the z direction, P is the pressure, and γ_{u} is the unburned-gas ratio of specific heats. In this formulation, $\dot{\mathcal{R}}_{\mathrm{f,z|dP}}$ is the time rate-of-change of $R_{\mathrm{f,z}}$ attributable to isentropic pressure change, dP. Eq. (7) is closely related to that derived for the axial post-reflected-shock gas velocity that results from isentropic pressure change, $u_{z|\mathrm{dP}}$, at an axial location L within the shock tube [39,40],

$$u_{z|\mathrm{dP}} \equiv \frac{-L}{\gamma_{\mathrm{u}}}\frac{1}{P}\frac{\mathrm{d}P}{\mathrm{d}t}. \tag{8}$$

Combining Eqs. (7) and (8), $\dot{\mathcal{R}}_{\mathrm{f,z|dP}}$ can then be related to $u_{z|\mathrm{dP}}$ through the ratio of length scales $R_{\mathrm{f,z}}$ and L,

$$\dot{\mathcal{R}}_{\mathrm{f,z|dP}} = \left(\frac{R_{\mathrm{f,z}}}{L}\right) u_{\mathrm{z|dP}}. \tag{9}$$

In the simple model adopted from [39,40], post-reflected-shock isentropic pressure change is assumed to manifest as a quasi-one-dimensional compression (or expansion) of the gas contained within the shock tube in the axial direction. As a result, while the pressure change imparts a non-zero effect on $R_{\mathrm{f,z}}$, the extent of the flame measured in the radial r directions (x and y in image coordinates), are unchanged by the isentropic process,

$$\dot{\mathcal{R}}_{\mathrm{f,r|dP}} = 0. \tag{10}$$

A brief discussion of higher-dimensional interactions that may result from the refraction of pressure waves through a flame is provided in Section 5.2.

5.1.2. Residual axial velocity

Using independently measured incident and reflected shock velocities, it is shown in [39,40] that the reflected shock strength at locations away from the end wall is inadequate to fully stagnate the core gas within region-5. In the presence of constant shock attenuation, the resulting residual axial velocity, $u_{z|res}$, changes nearly linearly with axial position z, measured from the end wall,

$$u_{z|res} \approx c_{res} z, \tag{11}$$

where c_{res} is a negative constant, such that the axial velocity is zero at the end wall and in the direction of the end wall for all other locations ($z > 0$) within the shock tube. From this same form, the rate of change imparted on the axial extent of the flame by the presence of the residual velocity gradient, $\dot{R}_{f,z|res}$, is proportional to z-directional radius,

$$\dot{\mathcal{R}}_{f,z|res} \equiv c_{res} R_{f,z}, \tag{12}$$

and can be related to the magnitude of the residual velocity at the measurement location,

$$\dot{\mathcal{R}}_{f,z|res} = \left(\frac{R_{f,z}}{L}\right) u_{z|res}. \tag{13}$$

The independence of the residual and isentropic-pressure-change velocities suggests that the residual velocity is not responsible for inducing the pressure change. As such, the residual core-gas flow field can reasonably be assumed axisymmetric and incompressible as a first-order approximation, such that the velocity components would be well-described by a scalar stream function, ψ, to enforce continuity [41],

$$u_{z|res} = \frac{1}{r}\frac{\partial \psi}{\partial r} \tag{14}$$

$$u_{r|res} = -\frac{1}{r}\frac{\partial \psi}{\partial z}. \tag{15}$$

In order to solve for the radial velocity field corresponding to the residual axial velocity, Eqs. (11) and (14) are first combined,

$$c_{res} z = \frac{1}{r}\frac{\partial \psi}{\partial r}, \tag{16}$$

allowing for integration to find a functional form for ψ,

$$\begin{aligned}\psi &= \int c_{res} z r \mathrm{d}r \\ &= \frac{c_{res} z r^2}{2} + f(z)\end{aligned} \tag{17}$$

An expression for $u_{r|res}$ can then be determined by substituting ψ from Eqs. (17) into Eq. (15),

$$\begin{aligned}u_{r|res} &= -\frac{1}{r}\frac{c_{res} r^2}{2} - \frac{1}{r}\frac{\mathrm{d}f(z)}{\mathrm{d}z} \\ &= -\frac{c_{res} r}{2} - \frac{1}{r}\frac{\mathrm{d}f(z)}{\mathrm{d}z}.\end{aligned} \tag{18}$$

The unknown function $f(z)$ is determined by evaluating Eq. (18) at r = 0,

$$\begin{aligned}u_{r|res}(r=0) \quad &= -\tfrac{c_{res}*0}{2} - \tfrac{1}{0}\tfrac{\mathrm{d}f(z)}{\mathrm{d}z} \\ 0 \quad &= \tfrac{\mathrm{d}f(z)}{\mathrm{d}z} = f(z).\end{aligned} \tag{19}$$

Providing the final result for the radial velocity field,

$$u_{r|res} = -\frac{c_{res} r}{2}. \tag{20}$$

The centroid of flames in the shock-tube environment remain nearly stationary in the x and y (radial) coordinates [39,40], consistent with the solution of Eq. (20) at $r = 0$. The perturbation rate of the radial flame extent induced by the residual velocity, $\dot{\mathcal{R}}_{f,r}$, is, therefore, equal to $u_{r|res}$ evaluated at the flame surface,

$$\dot{\mathcal{R}}_{f,r|res} = -\frac{c_{res} R_{f,r}}{2}. \tag{21}$$

Through substitution of Eqs. (12) and (13), the $\dot{\mathcal{R}}_{f,r|res}$ expression (Eq. (21)) can be cast in terms of $\dot{\mathcal{R}}_{f,z|res}$ or $u_{z|res}$,

$$\dot{\mathcal{R}}_{f,r|res} = -\dot{\mathcal{R}}_{f,z|res}\frac{R_{f,r}}{2R_{f,z}} \tag{22}$$

$$= -u_{z|res}\frac{R_{f,r}}{2L}. \tag{23}$$

5.1.3. Combined flow-field effect

Using the expressions derived in the previous subsections, relations for the combined post-shock flow-field effects on the observed burning velocity can be found as the sum of individual contributions from pressure change and residual velocity. Looking first to the axial direction, Eqs. (9) and (13) are combined,

$$\begin{aligned}\dot{\mathcal{R}}_{f,z} &= \dot{\mathcal{R}}_{f,z|dP} + \dot{\mathcal{R}}_{f,z|res} \\ &= \left(\frac{R_{f,z}}{L}\right) u_{z|dP} + \left(\frac{R_{f,z}}{L}\right) u_{z|res} \\ &= \left(\frac{R_{f,z}}{L}\right)\left(u_{z|dP} + u_{z|res}\right) \\ &\approx \left(\frac{R_{f,z}}{L}\right) u_{z,obs},\end{aligned} \tag{24}$$

where $u_{z,obs}$ in the final form is the observed, axial centroid velocity of the flame. By combining Eqs. (10) and (23), a similar expression can be found for the radial directions,

$$\begin{aligned}\dot{\mathcal{R}}_{f,r} &= \dot{\mathcal{R}}_{f,r|dP} + \dot{\mathcal{R}}_{f,r|res} \\ &= 0 - u_{z|res}\frac{R_{f,r}}{2L} \\ &= -\left(\frac{R_{f,r}}{L}\right)\left(\frac{u_{z|res}}{2}\right),\end{aligned} \tag{25}$$

through which the radial perturbation rate is seen to scale with the same R_f/L factor as the axial rate and the residual component of the axial velocity, $u_{z|res}$, calculated using measured shock velocities and normal shock relations.

Given the result that the signs of both $u_{z,obs}$ and $u_{z|res}$ are typically negative [39,40] (i.e. core gas flows towards end wall), it can readily be found that $\dot{\mathcal{R}}_{f,z} < 0$, leading to compression of flames in the Z direction, and $\dot{\mathcal{R}}_{f,r} > 0$, resulting in the radial stretching of flames. From this, it is seen that the direction of these perturbative effects are expected to occur in such a manner as would be required to induce the distortion seen in Fig. 7c.

Using values obtained from the highest-temperature experiment ($u_{z,obs} = -3.5$ m/s and $u_{z|res} = 2.3$ m/s), the magnitudes of the flow-field effects at a representative radius of 1 cm are found to be $\dot{\mathcal{R}}_{f,z} = -0.35$ m/s (Eq. (24)) and $\dot{\mathcal{R}}_{f,r} = 0.12$ m/s (Eq. (25)) in the Z and radial (X and Y) directions, respectively. This analysis has shown that, for the $T_5 = 935$ K case, flow-field effects would only explain about 0.5 m/s of the roughly 10 m/s propagation speed discrepancy documented in Fig. 10. Additionally, the flow-field mechanism only predicts relatively uniform compression and stretching, not the highly asymmetric distortion observed in the intermediate temperature ($T_5 = 784$ K, Fig. 7b) case. As such, while the framework for evaluating flow-field effects developed here does predict a distortion effect, the magnitude is found insufficient to explain the amount of distortion observed in the side-wall imaging results.

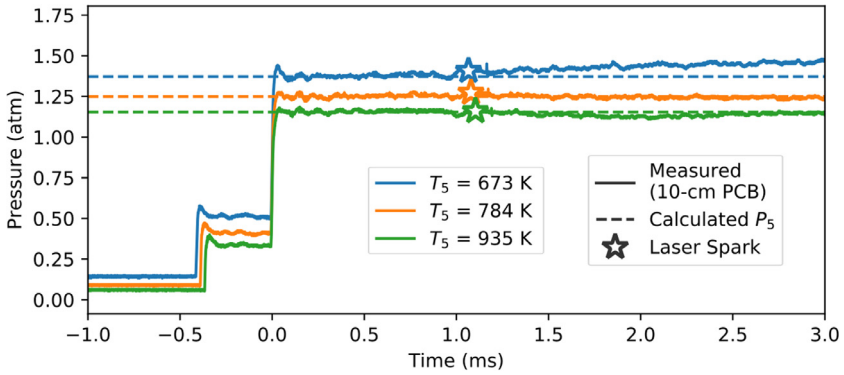

Fig. 11. Pressure–time histories recorded at the 10-cm plane during post-reflected-shock flame experiment; spark timings are shown as stars on the corresponding pressure data.

5.2. Pressure-wave–flame interactions

The flame front of a spherically expanding flame marks a discontinuity in properties between the unburned and burned gases. When a pressure wave passes through this discontinuity, the wave refracts, introducing effects beyond the quasi-1-D, axial compression of flames that arises from post-shock pressure rise as discussed in Section 5.1.1.

The effect of pressure waves on flames finds an analog in the widely studied shock-bubble interaction (SBI) configuration used as a basic configuration of impulsively accelerated fluid interfaces and the Richmyer-Meshkov instability [42]. Many investigations of SBI have been reported, both experimentally, using either dissimilar gases contained in soap bubbles [e.g. 43–45] or by studying the interaction of shock waves with expanding flames [e.g. 46–48], and through numerical simulations [e.g. 49–51]. Additional studies of shock-flame interactions have also been reported related to the deflagration-to-detonation transition (DDT) and flame-front instability [e.g. 52–57].

While the morphologies of the bubbles reported in the referenced works show some qualitative similarity to those of the distorted flames observed in this study, particularly that at the highest temperature (Fig. 7c), they are not directly comparable. Flames in this work, ignited following the passage of the reflected shock, would only be expected to interact with relatively weak pressure waves, not the discrete shock waves universally considered in SBI studies. This can be seen in the pressure–time histories from the shocked experiments (Fig. 11), recorded by a PCB pressure transducer at the 10-cm plane in which the flame is ignited. The incident and reflected shock waves are seen as the two step changes near times of -0.5 ms and zero, respectively. Following the reflected shock, all three experiments exhibit near-constant pressure through when the flame is ignited at about 1 ms; only gradual pressure changes are observed during the subsequent 2 ms, the time over which flame propagation is recorded.

After the flame is ignited, the lowest-temperature experiment (T_5 = 673 K) exhibits the most significant pressure change, rising somewhat steadily over the ensuing 2 ms. The pressure in the intermediate-temperature experiment (T_5 = 784 K) remains nearly constant through 3 ms post-reflected-shock, while the highest-temperature experiment (T_5 = 935 K) exhibits a slight decrease in pressure, followed by a return to the calculated P_5, in the time following the spark.

These trends in the pressure behavior run counter to that which would be expected if pressure-wave–flame interactions were a dominant effect in distorting flames. Specifically, the low-temperature experiment exhibits both the greatest post-shock pressure change and the least distortion. Conversely, the intermediate-temperature experiment that results in highly a distorted flame exhibits virtually no pressure change. As such, while the refraction of pressure waves through the burned gas would give rise to flame distortion, the recorded pressure data do not suggest that pressure waves of sufficient strength were present in the experiments shown to account for the observed flame distortion. Nevertheless, awareness of this mechanism does highlight the importance of ensuring pressure stability throughout flame experiments to prevent the occurrence of refracted-pressure-wave effects.

5.3. Localized double flames

A final, possible explanation for the anomalous distortion in the intermediate-temperature experiment (Fig. 7b) could be the presence of localized double flames existing over discrete portions of the flame surface. Numerous numerical studies, including that of Zhang et al. near the conditions of the present observations [58], have shown that spherical double-flame structures can exist at NTC-regime temperatures and drastically accelerate laminar burning velocities. Two-dimensional simulations of laser-induced ignition processes at high unburned-gas temperatures have since provided evidence that spark-induced non-uniformities in the vicinity of the plasma kernel may lead to double flames selectively forming over portions of the flame surface and lead to the development of aspherical distortion [59]. As only preliminary results of the numerical simulations have thus far been reported, and a conclusive explanation for the experimental observations cannot be ascertained from the presently available emission imaging results, additional study is warranted to explore the possible role of the local-double-flame phenomenon as a mechanism underlying the observed results.

6. Conclusion & future work

Dual-perspective imaging provided the first opportunity to evaluate the 3-D morphology of flames at high unburned-gas temperatures in a post-reflected-shock environment. While the previously assumed axis-symmetric structure is confirmed under static, constant-volume conditions and behind a reflected shock at a comparably low T_5 = 673 K, flames at higher temperatures exhibit axial distortion not unambiguously apparent from the end-wall perspective. The observed distortion provides a new understanding that previously reported flame structure featuring concentric rings of emission [10,11] can be attributed to end-wall images axially integrating emission through distorted flames.

Several candidate mechanisms were introduced and evaluated based on their ability to explain the observed flame distortion.

While the framework developed to predict the effect of a post-reflected-shock flow field predicts that it would induce the axial compression of flames, the expected magnitude was found to be too small to explain the present observations. Similarly, while the interaction of pressure waves with expanding flames would be expected to induce asymmetric distortion, the experimental pressure–time histories do not show evidence of the post-shock pressure changes that would be expected if pressure waves of any significance were present. Finally, based on the findings of recent numerical simulations, the presence of localized double flames was introduced as a mechanism that may be capable of explaining the asymmetric distortion observed in the intermediate temperature (T_5 = 784 K) experiment, though limits of the present experimental results, and preliminary nature of the simulations, precluded a detailed evaluation of the double-flame mechanism. As such, while a number of phenomena were evaluated, and some ruled out as a dominant cause, conclusive identification of the primary phenomenon underlying the observed axial distortion is identified as a topic requiring further study.

The morphology observations reported in this study demonstrate the value brought by the addition of side-wall imaging to shock-tube flame experiments. While the ability to perform side-wall imaging through a standard optical port was a key development enabling the present study, future experimental flame studies within a shock tube would greatly benefit from enhanced side-wall optical access to provide a wider FOV. Additionally, the extension of side-wall imaging to include a wider array of diagnostics, such as planar laser induced fluorescence (PLIF), could provide the additional experimental insights necessary to conclusively identify the physical phenomena that may be affecting high-temperature flames.

Finally, the addition of side-wall optical access presents an opportunity to enhance the fidelity of laminar flame speed measurements performed in the shock tube. While the present results illustrate that symmetry assumptions used in prior works are likely not valid under all conditions, the use of end- and side-wall imaging together presents an opportunity to more fully characterize the area and volume of flames even under conditions where distortion does occur. This could enable more accurate determinations of the mass burning flux of high-temperature flames and be an important step towards fully realizing the capabilities of the shock-tube flame speed method.

Declaration of Competing Interest

The authors declare that they have no known competing financial interests or personal relationships that could have appeared to influence the work reported in this paper.

Acknowledgments

This work was supported by the National Science Foundation under award number 1940865, contract monitor Dr. John Daily, and by the U.S. Army Research Office under grant number W911NF-17-1-0420, contract monitor Dr. Ralph Anthenien. A. J. Susa recognizes the U.S. Department of Defense for fellowship support through the NDSEG program. An additional thank you goes to LaVision for providing the HS-IRO-X intensifier that made this work possible.

Supplementary material

Supplementary material associated with this article can be found, in the online version, at 10.1016/j.combustflame.2021.111842

References

[1] W.C.F. Shepherd, The ignition of gas mixtures by impulsive pressures, Symp. Combust. Flame, and Expl. Phen., 3, Elsevier (1948), pp. 301–316.
[2] S. Bauer, Chemical kinetics in shock tubes, Science 141 (3584) (1963) 867–879.
[3] W. Tsang, A. Lifshitz, Shock tube techniques in chemical kinetics, Annu. Rev. Phys. Chem. 41 (1) (1990) 559–599.
[4] R.K. Hanson, D.F. Davidson, Recent advances in laser absorption and shock tube methods for studies of combustion chemistry, Prog. Energy Combust. Sci. 44 (2014) 103–114.
[5] A.M. Ferris, A.J. Susa, D.F. Davidson, R.K. Hanson, High-temperature laminar flame speed measurements in a shock tube, Combust. Flame 205 (2019) 241–252.
[6] T. Spiglanin, A. Mcilroy, E. Fournier, R. Cohen, J. Syage, Time-resolved imaging of flame kernels: laser spark ignition of H_2/O_2/Ar mixtures, Combust. Flame 102 (3) (1995) 310–328.
[7] D. Bradley, C.G.W. Sheppard, I.M. Suardjaja, R. Woolley, Fundamentals of high-energy spark ignition with lasers, Combust. Flame 138 (1–2) (2004) 55–77.
[8] T.X. Phuoc, Laser-induced spark ignition fundamental and applications, Opt. Laser Eng. 44 (5) (2006) 351–397.
[9] C. Dumitrache, A.P. Yalin, Gas dynamics and vorticity generation in laser-induced breakdown of air, Opt. Express 28 (4) (2020) 5835–5850.
[10] A.J. Susa, A.M. Ferris, D.F. Davidson, R.K. Hanson, Experimental observation of negative temperature dependence in *iso*-octane burning velocities, AIAA J. 57 (10) (2019) 4476–4481.
[11] A.J. Susa, A.M. Ferris, D.F. Davidson, R.K. Hanson, Experimental measurement of laminar burning velocity of *n*-heptane at variable extents of reactions in a shock tube, 32nd Int. Symp. Shock Waves, International Shock Wave Institute (2019), pp. 917–925.
[12] Y. Ju, Understanding cool flames and warm flames, Proc. Combust. Inst. 38 (1) (2021) 83–119.
[13] S.G. Saytzev, R.I. Soloukhin, Study of combustion of an adiabatically-heated gas mixture, Symp. (Int.) Combust. 8 (1) (1961) 344–347.
[14] J. Meyer, A. Oppenheim, On the shock-induced ignition of explosive gases, Symp. (Int.) Combust. 13 (1) (1971) 1153–1164.
[15] D. Vermeer, J. Meyer, A. Oppenheim, Auto-ignition of hydrocarbons behind reflected shock waves, Combust. Flame 18 (3) (1972) 327–336.
[16] A. Sasoh, J. Maemura, S. Hirakata, K. Takayama, J. Falcovitz, Diaphragm rupture. impingement by a conically-nosed, ram-accelerator projectile, Shock Waves 9 (1) (1999) 19–30.
[17] C. Lee, S. Vranckx, K.A. Heufer, S.V. Khomik, Y. Uygun, H. Olivier, R.X. Fernandez, On the chemical kinetics of ethanol oxidation: shock tube, rapid compression machine and detailed modeling study, Z. Phys. Chem. 226 (1) (2012) 1–28.
[18] A.J. Susa, L. Zheng, R.K. Hanson, Schlieren-based measurements of propane flame speeds at extreme temperatures, 12th US Natl. Combust. Meet. (2021), p. 1G05.
[19] V.A. Troutman, C.L. Strand, M.F. Campbell, A.M. Tulgestke, V.A. Miller, D.F. Davidson, R.K. Hanson, High-speed OH^* chemiluminescence imaging of ignition through a shock tube end-wall, Appl. Phys. B 122 (3) (2016) 56.
[20] S. Zabeti, M. Fikri, C. Schulz, Reaction-time-resolved measurements of laser-induced fluorescence in a shock tube with a single laser pulse, Rev. Sci. Instrum. 88 (11) (2017) 115105.
[21] P. Niegemann, M. Fikri, I. Wlokas, M. Röder, C. Schulz, Methodology for the investigation of ignition near hot surfaces in a high-pressure shock tube, Rev. Sci. Instrum. 89 (5) (2018) 055111.
[22] M. Figueroa-Labastida, A. Farooq, Simultaneous lateral and endwall high-speed visualization of ignition in a circular shock tube, Combust. Flame 214 (2020) 263–265.
[23] E. Ninnemann, O. Pryor, S. Barak, S. Neupane, Z. Loparo, A. Laich, S.S. Vasu, Reflected shock-initiated ignition probed via simultaneous lateral and endwall high-speed imaging with a transparent, cylindrical test-section, Combust. Flame 224 (2021) 43–53.
[24] M.F. Campbell, A.M. Tulgestke, D.F. Davidson, R.K. Hanson, A second-generation constrained reaction volume shock tube, Rev. Sci. Instrum. 85 (5) (2014) 055108.
[25] J. Carpentier, Improvements in enlarging or like cameras, 1901, (GB Patent).
[26] T. Scheimpflug, Improved method and apparatus for the systematic alteration or distortion of plane pictures and images by means of lenses and mirrors for photography and for other purposes, 1904, (GB patent).
[27] M.F. Campbell, K.G. Owen, D.F. Davidson, R.K. Hanson, Dependence of calculated postshock thermodynamic variables on vibrational equilibrium and input uncertainty, J. Thermophys. Heat Transf. 31 (3) (2017) 586–608.
[28] G. Van Rossum, F.L. Drake Jr, Python Tutorial, 620, Centrum voor Wiskunde en Informatica Amsterdam, 1995.
[29] S. van der Walt, J.L. Schönberger, J. Nunez-Iglesias, F. Boulogne, J.D. Warner, N. Yager, E. Gouillart, T. Yu, the scikit-image contributors, Scikit-image: image processing in Python, PeerJ 2 (2014) e453.
[30] P. Virtanen et al, Scipy 1.0: fundamental algorithms for scientific computing in Python, Nat. Methods 17 (2020) 261–272.
[31] J. Canny, A computation approach to edge detection, IEEE Trans. Pattern Anal. Mach. Intell. 8 (6) (1986) 670–700.
[32] P.-S. Liao, T.-S. Chen, P.-C. Chung, et al., A fast algorithm for multilevel thresholding, J. Inf. Sci. Eng. 17 (5) (2001) 713–727.

[33] K. Wu, E. Otoo, A. Shoshani, Optimizing connected component labeling algorithms, Medical Imaging 2005: Image Processing, 5747, International Society for Optics and Photonics (2005), pp. 1965–1976.
[34] A. Savitzky, M.J. Golay, Smoothing and differentiation of data by simplified least squares procedures, Anal. Chem. 36 (8) (1964) 1627–1639, doi:10.1021/ac60214a047.
[35] F. Halter, Z. Chen, G. Dayma, C. Bariki, Y. Wang, P. Dagaut, C. Chauveau, Development of an optically accessible apparatus to characterize the evolution of spherically expanding flames under constant volume conditions, Combust. Flame 212 (2020) 165–176.
[36] F.W. Stevens, A Constant Pressure Bomb, Technical Report, National Advisory Committee for Aeronautics, 1923.
[37] M.P. Burke, Z. Chen, Y. Ju, F.L. Dryer, Effect of cylindrical confinement on the determination of laminar flame speeds using outwardly propagating flames, Combust. Flame 156 (4) (2009) 771–779.
[38] T.X. Phuoc, Laser spark ignition: experimental determination of laser-induced breakdown thresholds of combustion gases, Opt. Commun. 175 (4–6) (2000) 419–423.
[39] A.J. Susa, R.K. Hanson, Flame-drift velocimetry and flame morphology measurements with dual-perspective imaging in a shock tube, 12th US Natl. Combust. Meet. (2021), p. 1G13.
[40] A.J. Susa, R.K. Hanson, Flame-image velocimetry: non-intrusive characterization of post-reflected-shock velocities in a shock tube, Exp. Fluids (In review).
[41] C.K. Batchelor, G. Batchelor, An Introduction to Fluid Dynamics, Cambridge university press, 2000, p. xviii.
[42] D. Ranjan, J. Oakley, R. Bonazza, Shock-bubble interactions, Annu. Rev. Fluid Mech. 43 (2011) 117–140.
[43] J.-F. Haas, B. Sturtevant, Interaction of weak shock waves with cylindrical and spherical gas inhomogeneities, J. Fluid Mech. 181 (1987) 41–76.
[44] D. Ranjan, J.H. Niederhaus, J.G. Oakley, M.H. Anderson, R. Bonazza, J.A. Greenough, Shock-bubble interactions: features of divergent shock-refraction geometry observed in experiments and simulations, Phys. Fluids 20 (3) (2008) 036101.
[45] N. Haehn, D. Ranjan, C. Weber, J. Oakley, D. Rothamer, R. Bonazza, Reacting shock bubble interaction, Combust. Flame 159 (3) (2012) 1339–1350.
[46] G. Markstein, A shock-tube study of flame front-pressure wave interaction, Symp. (Int.) Combust. 6 (1) (1957) 387–398.
[47] J. Picone, E. Oran, J. Boris, T. Young Jr, Theory of Vorticity Generation by Shock Wave and Flame Interactions, Technical Report, Naval Research Lab, 1984.
[48] H. Yang, M.I. Radulescu, Dynamics of cellular flame deformation after a head-on interaction with a shock wave: reactive Richtmyer–Meshkov instability, J. Fluid Mech. 923 (2021).
[49] M.W. Evans, F.H. Harlow, B.D. Meixner, Interaction of shock or rarefaction with a bubble, Phys. Fluids 5 (6) (1962) 651–656.
[50] J. Picone, J. Boris, Vorticity generation by shock propagation through bubbles in a gas, J. Fluid Mech. 189 (1988) 23–51.
[51] J.J. Quirk, S. Karni, On the dynamics of a shock–bubble interaction, J. Fluid Mech. 318 (1996) 129–163.
[52] Y. Ju, A. Shimano, O. Inoue, Vorticity generation and flame distortion induced by shock flame interaction, Symp. (Int.) Combust. 27 (1) (1998) 735–741.
[53] G. Thomas, R. Bambrey, C. Brown, Experimental observations of flame acceleration and transition to detonation following shock-flame interaction, Combust. Theory Model. 5 (4) (2001) 573.
[54] V. Gamezo, A. Khokhlov, E. Oran, Effects of wakes on shock-flame interactions and deflagration-to-detonation transition, Proc. Combust. Inst. 29 (2) (2002) 2803–2808.
[55] E. Oran, V. Gamezo, A. Khokhlov, Effects of boundary layers and wakes on shock-flame interactions and ddt, 40th AIAA Aerospace Sciences Meeting & Exhibit (2002), p. 776.
[56] G. Dong, B. Fan, J. Ye, Numerical investigation of ethylene flame bubble instability induced by shock waves, Shock Waves 17 (6) (2008) 409–419.
[57] Y. Zhu, L. Gao, Effect of reactive gas mixture distributions on the flame evolution in shock accelerated flow, Acta Astronaut. 179 (2021) 484–494.
[58] T. Zhang, A.J. Susa, R.K. Hanson, Y. Ju, Studies of the dynamics of autoignition assisted outwardly propagating spherical cool and double flames under shock-tube conditions, Proc. Combust. Inst. 38 (2) (2021) 2275–2283.
[59] T. Zhang, A.J. Susa, R.K. Hanson, Y. Ju, Two-dimensional simulation of cool and double flame formation induced by the laser ignition under shock-tube conditions, 12th US Natl. Combust. Meet. (2021), p. 1G06.